

A General-Purpose Transit Simulator for Arbitrary Shaped Objects Orbiting Stars

USHASI BHOWMICK^{1,2} AND VIKRAM KHAIRE²

¹*Space Applications Centre, Indian Space Research Organization, Ahmedabad, India*

²*Indian Institute of Space Science and Technology, Thiruvananthapuram, Kerala 695547, India*

ABSTRACT

We present a versatile transit simulator aimed at generating light curves for arbitrarily shaped objects transiting stars. Utilizing a Monte Carlo algorithm, it accurately models the stellar flux blocked by these objects, producing precise light curves. The simulator adeptly handles realistic background stars, integrating effects such as tidal distortions and limb darkening, alongside the rotational dynamics of transiting objects of arbitrary geometries. We showcase its wide-ranging utility through successful simulations of light curves for single and multi-planet systems, tidally distorted planets, eclipsing binaries and exocomets. Additionally, our simulator can simulate light curves for hypothetical alien megastructures of any conceivable shape, providing avenues to identify interesting candidates for follow-up studies. We demonstrate applications of the simulator in modeling a Dyson Swarm in construction, Dyson rings and Dyson disks, discussing how tidally locked Dyson disks can be distinguished from planetary light curves.

1. INTRODUCTION

The discovery of the first exoplanet 51 Pegasi-b (Mayor & Queloz 1995) in year 1995 has led to the emergence of numerous instruments on the ground and in space to identify and characterize exoplanets. With the launch of the Kepler Space Telescope (Kepler) in 2009 (Koch et al. 2010; Borucki et al. 2010) followed by Transiting Exoplanet Survey Satellite (TESS) in 2018 (Ricker et al. 2015), the transit method became the most popular and efficient means to find exoplanets with more than 4000 exoplanet discoveries (NASA exoplanet science institute 2010). With the increasing sensitivity and precision of instruments, research has shifted from merely identifying exoplanets to studying detailed characteristics of them.

Transit photometry has uncovered signatures of many interesting phenomena beyond the detection of exoplanets and eclipsing binaries. This technique has been instrumental in identifying features such as starspots (e.g., Vivekananda Rao et al. 1991; Giles et al. 2017; Tregloan-Reed et al. 2013), and signatures of tidal interactions between host stars and exoplanets (e.g., Kramm et al. 2012; Barros et al. 2022; Albrecht et al. 2012) leading to significant growth in the sub-field of Asteroseismology

(e.g., Bastien et al. 2013; Yu et al. 2018; Campante et al. 2016). The study of transit timing variations has led to the discovery of further non-transiting planets (e.g., Steffen et al. 2012; Ballard et al. 2011; McKee & Montet 2024), orbital decay (e.g., Maciejewski et al. 2016; Harre & Smith 2023) and apsidal precession - a gravitational phenomenon that causes the orbit of a planet to gradually rotate over time (e.g., Baycroft et al. 2023; Bernabò et al. 2024). This effect, along with other findings like disintegrating planets (Rappaport et al. 2012; Brogi et al. 2012a), exocomets (e.g., Ferlet et al. 1987; Lecavelier Des Etangs et al. 1996; Kiefer et al. 2023) and exomoon candidates (e.g., Kipping et al. 2022), has expanded our understanding of the diversity and complexity of planetary systems. Additionally, transit photometry has detected anomalous transit signals that have sparked interest in the search for technosignatures for the evidence of advanced civilizations (e.g., Boyajian et al. 2016; Lipman et al. 2019; Zuckerman et al. 2024; Chakraborty et al. 2020).

Technosignatures, which are evidence of technology that could not arise from natural processes and instead imply the presence of intelligent life, fall within the scope of the Search for Extraterrestrial Intelligence (SETI; e.g., Tarter 2001, 2007; Lebofsky et al. 2019). These signatures encompass a wide range of indicators, from astroengineering projects and signals of planetary origin to interstellar space probes, offering concrete evidence of extraterrestrial civilizations and potentially transform-

ing our understanding of our place in the universe (e.g., Haqq-Misra et al. 2022; Wright et al. 2022).

Astroengineering projects, in particular, involve the construction of large-scale megastructures, with the Dyson Sphere (Dyson 1960) being a prime example. This theoretical construct is envisioned as a massive shell surrounding a star to capture its energy output. The feasibility, sustainability, and potential designs of such megastructures have been explored in various studies (e.g., Smith 2022; Semiz & Oğur 2015; Wright 2020; Loeb 2023), alongside concepts like stellar engines (Caplan 2019; Svoronos 2020) designed to propel stars. The presence of these megastructures could manifest as anomalies in the observed transit light curves, deviating from the patterns expected from spherical planets due to their unique geometries. Detecting such distortions requires careful analysis to distinguish them from natural phenomena affecting transit light curves. The role of transiting megastructures as key technosignatures in SETI research underscores the need for advanced techniques to identify unmistakable signs of extraterrestrial engineering (see for e.g., Arnold 2005; Wright et al. 2016).

Considering the wide range of observed transits and the speculative nature of megastructures, we have developed a versatile numerical tool designed to simulate the transit light curves of any objects orbiting stars. Our approach employs a Monte Carlo simulation to numerically generate transit light curves for transiting objects with arbitrary geometry. Previously, with a similar approach Carado & Knuth (2020), used Monte Carlo simulation to model transits and reflected light curves of non-spherical planets. Additionally, other methods are being used for modeling the transits of non-spherical structures (e.g., Sandford & Kipping 2019; Zuluaga et al. 2022; Arkhypov et al. 2021; Nachmani et al. 2022). This paper details our methodology for simulating transits, demonstrating its application across a variety of natural transiting phenomena and megastructure concepts.

The paper is organized as follows. Section 2 describes the method used in our simulator and all its considerations. In section 3, we study the performance of the simulator in modeling natural transits such as those of single planets, multi-planetary systems, systems experiencing tidal distortions, and exocomets. In section 4, we showcase the ability of our simulator to model a range of megastructures, including Dyson swarms, Dyson rings, and Dyson disks, with a particular focus on the detectability of Dyson disks. Finally Section 5 provides a summary of the paper’s main results.

2. SIMULATING TRANSIT LIGHT CURVE

2.1. Brief Introduction of Transits

A transit occurs when an orbiting object comes in front of the star, with respect to the line of sight. The object blocks some light of the star; hence we observe a dip in the flux. The time taken by the object to complete one orbit around the star is known as the transit period. The time that the object orbits in front of the star while blocking the flux is known as the transit duration. The ingress and egress periods denote the time intervals when the object partially obscures the star as it enters or exits the transit phase, respectively.

Observed light curves (i.e flux values of the star as a function of time) are analyzed for the presence of a transit. If a periodic dip signature is detected then it is called a transit. Once the periodicity of a transit is determined, the light curve is often phase-folded over the transit period to obtain high signal-to-noise data for the transit. It is often useful to plot a light curve in terms of its phase where one transit period corresponds to a variation of phase angle(θ) from $-\pi$ to π .

These transit light curves can be fitted to study the characteristics of the planet using analytic models. One such widely used model is provided in Mandel & Agol (2002). It models the transit of a planet assuming the planet as an opaque dark sphere and the star as a spherical body. This model describes the light curve of a transit using five parameters. These parameters include the relative size of the planet with respect to the star R_{pl}/R_{st} where R_{pl} and R_{st} are the radius of the planet and the radius of the star respectively, which determines the depth of the transit; the relative distance of the planet to the star i.e the semi-major axis of the orbit R_{orb} with respect to the stellar radius (R_{orb}/R_{st}), which governs the width of the transit duration with respect to the transit period; and the impact parameter (b) which is the center-to-center distance between the planet and the star projected along the line of sight. The remaining two parameters u_1 and u_2 are limb darkening coefficients (see Eq. 2) that are crucial for modeling the stellar limb darkening.

The limb darkening is a phenomenon due to which a star appears brighter at the center and dimmer at the edges. This is because at the center of the projected star in the sky, the light seen by us is arriving from all the layers including the the core of the star which is at a hotter temperature, and therefore it seems bright. At the edges of the star, the flux received by us is arising from the cooler outer levels of the stellar atmosphere, therefore the star appears dimmer. There are many functional forms used to model the limb-darkening phenomena. However, in this work, we use the quadratic

limb darkening law,

$$\frac{I(\mu)}{I_0} = 1 - u_1(1 - \mu) - u_2(1 - \mu)^2, \quad (1)$$

and the non-linear limb darkening law (Claret 2000),

$$\frac{I(\mu)}{I_0} = 1 - a(1 - \mu^{1/2}) - b(1 - \mu) - c(1 - \mu^{3/2}) - d(1 - \mu^2). \quad (2)$$

Here, $I(\mu)$ is the intensity of the star at $\mu = \cos \phi$ i.e. the cosine of the angular separation (ϕ) of a point with respect to the center of the star, I_0 is the intensity at the center of the star, and $u_1, u_2, a, b, c,$ and d are the limb darkening coefficients.

2.2. Arbitrary Transit Model

In order to extend the transit model to a generalized shape of the transit object, we need to invoke the basic principle of transit. The transit principle states that the relative change in the observed flux is proportional to the relative area of the blocking object with respect to the area of the star projected to the sky plane perpendicular to the line of sight, as given by

$$\frac{\Delta F}{F} = \frac{A_{pl}}{A_{st}}. \quad (3)$$

Here A_{pl} refers to the projected area of the blocking object overlapping with the background object, and A_{st} refers to the projected area of the star or background object. An object with a bigger area of projection causes a deeper dip. In order to construct the light curve, we need to evaluate $\Delta F/F$ as a function of time (t) i.e. $A_{pl}(t)/A_{st}$. For example, during ingress and egress, the transiting object is not fully in front of the star. Hence the area to be considered corresponds to the part that overlaps the star when both the object and star are projected on the sky plane. In the case of planets, for which spherical geometry is an excellent approximation, the projected area on the sky plane is always a circle. Therefore, it is possible to calculate $A_{pl}(t)/A_{st}$ analytically for planets (e.g. see Mandel & Agol 2002). However, for an arbitrary object in transit, we have to switch to numerical methods to evaluate $A_{pl}(t)/A_{st}$. To do this, we utilize a standard Monte Carlo technique as described below.

Consider an arbitrary outer shape and an arbitrary transiting system as shown in Fig. 1 (A). We have a background stationary shape (a circle), and a moving foreground shape (a hollow pentagon). If we sample a random point on the circle, the probability of the point being placed within the transiting shape is equal to the ratio of the overlapping area of the shape (A_{pl}) to the background shape (A_{st}). This is given as,

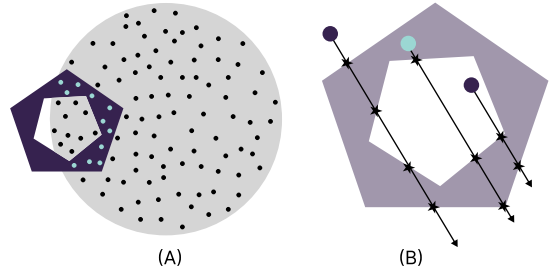


Figure 1. Demonstration of the Monte-Carlo technique for numerical area calculation. (A) shows an outer circle and an inner shape, with each point having a certain probability of lying on the inside shape. A large number of sampled points is needed for an accurate estimate of the overlapped area between the background circle and foreground shape. (B) shows the ray casting technique, which is a method to evaluate whether a point lies inside or outside a particular shape by drawing a ray in any direction and calculating its intersection with the edges of the shape. An even number of intersections imply that the point is outside the shape, and an odd number of intersections means that the point is inside the shape.

$$P = \frac{A_{pl}}{A_{st}}$$

To evaluate A_{pl}/A_{st} , we need to evaluate P . To achieve this, we need to sample a number of random points inside the background shape. Then we count the number of points that simultaneously lie inside the inner shape, considering only the overlapping area. The fraction of such points gives us the value of P . This in turn gives us A_{pl}/A_{st} and therefore the normalized light curve $\Delta F/F$. The following subsections describe the exact algorithm, which is also demonstrated graphically in Fig. 2.

2.3. Modelling a stellar source with limb darkening

In this work, we assume the shape of the background star to be a sphere with the flexibility to include a more general case of a triaxial ellipsoid star. Even though the analogy of arbitrary shapes of transiting objects can be extended to arbitrarily shaped luminous objects as well, for the purpose of this work, only sphere and triaxial ellipsoids have been considered for modeling the stellar source.

For a spherical star, we need to sample a large number of uniform random points within the projected area of the star on the sky plane i.e a circle. This requires two sets of random numbers that represent the polar coordinates. One represents radius r , ranging from 0 to R_{st} and the other represents the angle (θ_s), ranging from 0 to 2π . A distribution that is uniform over the area of the circle is not uniform in r and θ_s . Since area is

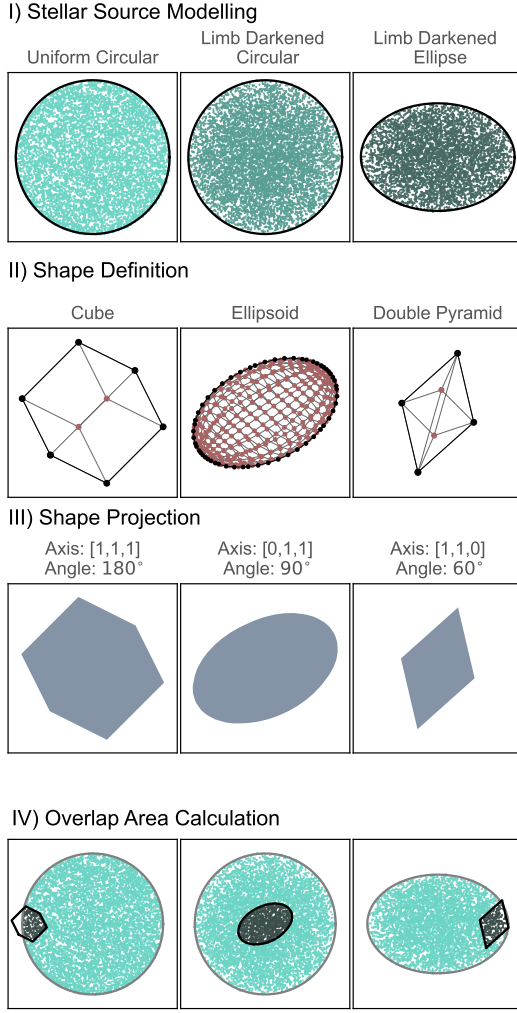


Figure 2. Workflow of the transit simulation. (I) shows the modeling of the stellar source with a uniform, limb-darkened, and limb-darkened elliptical distribution. (II) shows the definition of three arbitrary shapes (cube, ellipsoid, double pyramid) rotated by a random angle around an axis, using corners and edges. (III) shows the subsequent projected sub-shape. In (IV), the sub-shape is put in orbit around the star and the points inside the sub-shape are highlighted. The fraction of in points to out is used to calculate the area of overlap.

proportional to r^2 , we need a square root distribution over r to obtain a uniform distribution over the circular area. Taking this into account we generate uniformly distributed points in a circle as shown in the first panel in Fig. 2 (I).

However, because of the limb darkening, the flux from the projected star is brighter at the center and dimmer at the edges. To include this in our simulation, we need to modify our assumption that the host star is represented as uniformly distributed points over a circle. In turn, our distribution must follow the intensity pat-

tern prescribed by the chosen limb darkening law. Our model can accept any limb-darkening law when written in the form of a cumulative distribution function. To generate the distribution, we use the inversion method as described below.

For our analysis, we select the quadratic limb darkening law (Eq. 1) and convert the intensity to a cumulative distribution function (CDF) in terms of the radius r of the circle,

$$CDF = \frac{1}{k} \left[(1 - u_1 - 2u_2)r^2 + \frac{1}{2}u_2r^4 + \frac{2}{3}(u_1 + 2u_2)\{(1 - r^2)^{3/2} - 1\} \right], \quad (4)$$

where,

$$k = 1 - \frac{u_1}{3} - \frac{u_2}{6}. \quad (5)$$

To obtain the correct distribution for r , we need to invert the CDF, by generating a uniform distribution and solving for r . The resulting distribution of random points obtained using the above prescription is illustrated in the second panel of Fig. 2(I). The sampling points show less density at the edges representative of the dimmer edges of the projected star to mimic the limb darkening.

As an extension of the algorithm, we also describe a more general stellar shape: a triaxial ellipsoid with three axes r_a, r_b, r_c . For that instead of a circular projection, we need an elliptical projection. To apply the limb darkening formula for elliptical shape, we generate a circular limb darkened distribution with $r = 1$ and then scale it according to θ_s (between r_1 and r_2 , the two axes of the projection). This gives us an elliptical projection as demonstrated in the right-hand panel of Fig. 2 (I).

2.4. Modelling the Orbit

To calculate the flux change at any time in the transit period we need to locate the object in its orbit. For that, we set the orbital parameters for the transit. For a single planet or any arbitrary object simulation, we need to choose an orbital distance and an inclination towards the observer's line of sight. For a multi-planet system, we need the relative orbital velocity and a phase offset between the planets.

We sample the total phase $\theta = (0, 2\pi)$ with a chosen resolution i.e. the cadence of the transit. This phase angle (θ) is a measure of a fraction of the orbital period. For circular orbits with constant angular velocity, the phase angle is equal to the orbital phase angle (Θ). The orbital phase angle is a phase value corresponding to the location of the planet in its orbit at a certain time.

In order to model an eccentric orbit instead of a circular one, we use the Kepler equation for the distance

(r) of the object with respect to the star in the orbit, which is given by,

$$r = \frac{a(1 - e^2)}{1 + e \cos\Theta}, \quad (6)$$

where e is the eccentricity of the orbit and a is the semi-major axis length. For eccentric orbits, the angular velocity of the orbiting body is not constant, therefore the phase angle θ is not equal to the orbital phase angle Θ . We account for this by calculating the orbital phase angle (Θ) for each phase point using equations given below:

$$\Omega = \frac{2\pi a^2 \sqrt{1 - e^2}}{r^2}, \quad (7)$$

$$\Omega = \frac{\Delta\Theta}{\Delta t}, \quad \frac{\Delta\theta}{2\pi} = \frac{\Delta t}{P}.$$

Here Ω is the orbital velocity and P refers to the orbital period of the system. Using Ω for each point, we can use the equations given above and calculate the Θ for each value of θ from 0 to 2π . Additionally, we also need the periapsis offset i.e. an angle that determines the orientation of the semi-major axis with respect to the line of sight. This along with Ω for each point allows us to determine the position of the object within its orbit, enabling us to calculate the decrease in flux at each orbital point by modeling the object's shape and following our Monte-Carlo method as described below.

2.5. Modelling of Transiting Object

We define a shape for the transiting object in terms of the coordinates of its corners. Arbitrary 3D shapes are defined by a set of three dimensional coordinates and their connected edges. We calculate the projection of the shape to our line of sight. We evaluate the projection of the object at each point in transit to generate a set of 2D sub-shapes at each point in the transit. If our shape also includes rotation, we alter coordinates accordingly by making use of rotation matrices. This is shown in Fig. 2 (rows II and III), where we take three different shapes, rotate them, and calculate their projections. The projected sub-shape is a list of those corners which form the outer boundary of the projection. These sub-shapes are then subjected to a Monte-Carlo sampling as described below.

2.6. Monte-Carlo Simulation

The sub-shape is translated to its position in the orbit. Then we calculate the overlapped area using the Monte-Carlo technique. For each of the randomly sampled points in the star, we evaluate whether it lies in the interior or the exterior of the shape. If the transiting object is a circle as in the case of planets, this amounts to

evaluating the distance d between the point in question from the center of the transiting circle. If the distance d of the point is greater than the radius r of the circle (i.e., $d > r$) then the point is outside the circle, and if $d < r$ the point is inside the circle. For other shapes, however, the algorithm is not that simple, and instead, we use a technique called ray casting to determine if the points are inside the shape or not.

Ray casting is a concept that is used to calculate whether a point lies inside or outside a 2D shape under the assumption that any closed curve can be approximated as a set of coordinates. Consider a random point and draw a ray extending from it in any (chosen) direction. If the point lies inside the shape, then the ray crosses the boundary of the curve an odd number of times (see panel B of Fig. 1). If the point lies outside, it crosses the boundary for an even number of times. For our algorithm, we draw horizontal, right-seeking rays from each point and calculate their intersections to the edges of the shape. This determines whether each point lies in or out of the shape. The fraction of points lying inside the shape gives us the value of $\Delta F/F$ for that point in the trajectory, as is depicted in Fig. 2 (row IV). The methodology described above can be used to simulate the transit of any arbitrary shape orbiting a host star.

3. MODELLING NATURAL TRANSITS: PLANETS, TIDAL DISTORTIONS, AND EXOCOMETETS

In this section, we validate our Monte Carlo technique used in the transit simulator by modeling several natural transit phenomena, including single and multi-planet transits, transits around tidally distorted stars, and exocomets. We compare our models to those reported in the literature, demonstrating that our technique is not only robust but also versatile. The following subsections present these examples.

3.1. A Single Exoplanet Transit and Error Analysis

To validate our numerical simulator we test it on a simple exoplanet transit. We simulate a planet with an arbitrary set of parameters (as $R_{pl} = 0.12R_{st}$, $R_{orb} = 2R_{st}$, $u_1 = 0.3$ and $u_2 = 0.2$) and compare it to the analytical transit model of Mandel & Agol (2002) in Fig. 3. Our simulation matches perfectly with the analytical model as shown in the top panel of Fig. 3 with overlapping curves. The difference between our simulation and the model is minimal, within 0.5%, as indicated in the residual plot in the bottom panel of Fig. 3. The close match between the analytical model and our simulation confirms the accuracy and reliability of our technique. This minor difference arises from Monte-Carlo noise as explained below.

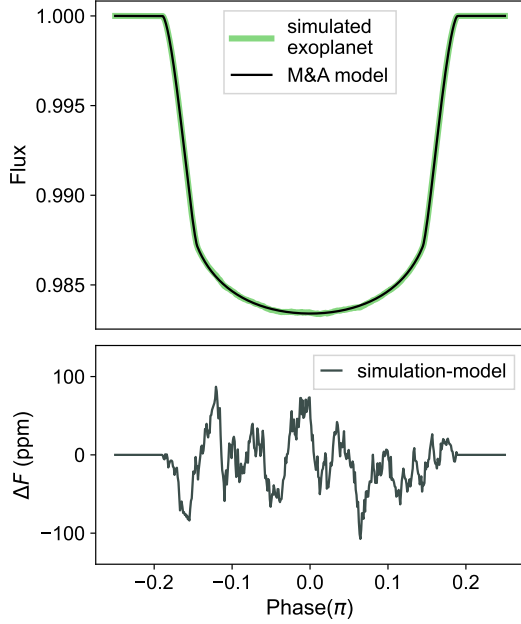


Figure 3. Comparison of the simulation with the standard model for a transiting exoplanet around a limb-darkened star. Simulated parameters are: $R_{pl} = 0.12R_{st}$, $R_{orb} = 2R_{st}$, $u_1 = 0.3$ and $u_2 = 0.2$. The top panel shows the simulation and the analytical model (overlapping) of Mandel & Agol (2002). The bottom panel plots the residuals (simulation - model) arising due to Monte-Carlo noise. The residuals are less than 0.5% of the transit depth.

The performance of the simulator depends on two factors, the first is the frame resolution i.e., the number of points used to model the orbit, and the second is Monte-Carlo resolution i.e., the number of points used to sample the star. The performance can be measured by evaluating the Monte-Carlo noise of the output light curve. To determine the Monte-Carlo noise, we calculate the root mean square (RMS) of the difference between two runs of the simulations performed with different sets of random numbers. We repeat this exercise for different frame resolutions and Monte Carlo resolutions. In Fig. 4, we show the variation of Monte-Carlo noise with frame (top panel) and Monte-Carlo resolutions (bottom panel). In the top panel of Fig. 4, the Monte-Carlo resolution is fixed at 10^5 points, while the frame resolution is variable. We observe that the RMS error flattens out to a fixed value of 3.12×10^{-4} for a frame resolution greater than 500 (i.e., $\Delta\theta < 0.0126$) corresponding to the noise of the sampled distribution. In the bottom panel, we keep the number of frames constant at 500 and vary the Monte-Carlo resolution. The RMS error decreases with increasing number of sampled points following characteristic $1/\sqrt{n}$ decrement as illustrated by

a fit to the RMS error in the bottom panel of Fig. 4 (the solid line).

In conclusion, our error analysis demonstrates that while the frame resolution significantly impacts the precision of the simulated light curve, achieving a frame resolution above 500 points or $\Delta\theta < 0.0126$ effectively minimizes Monte Carlo noise, stabilizing the RMS error. Additionally, the observed trend in RMS error reduction with increasing Monte Carlo resolution underscores the inherent efficiency of Monte Carlo simulations in modeling the light curves.

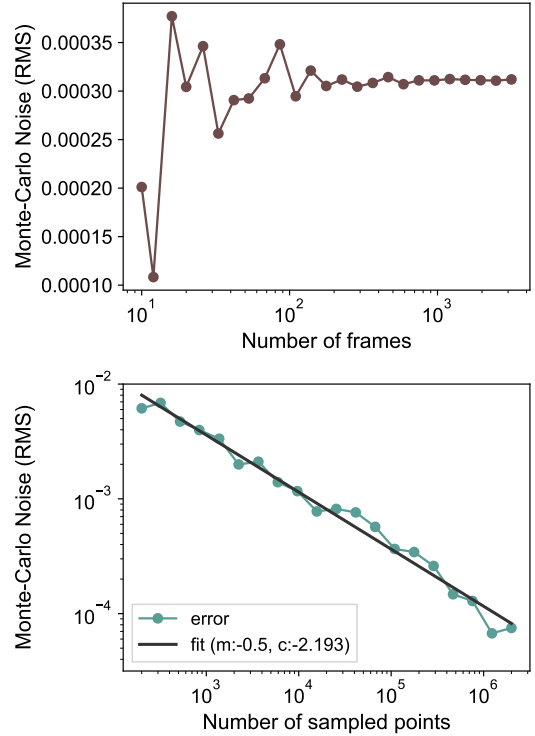


Figure 4. Convergence of Monte-Carlo simulation. The top panel shows the variation of Monte-Carlo noise with changing frame resolution with a fixed sampling resolution of 10^5 . The RMS error flattens out to a fixed value of 3.12×10^{-4} . The bottom panel shows the variation of Monte-Carlo noise with sampling resolution, for a fixed frame resolution of 500. The plot is linear in the log-log scale, as represented by the best-fit line ($y = mx + c$). The slope of this line is $m = -0.5$, which is characteristic of a Monte-Carlo distribution.

3.2. A multi-planetary system: Trappist-I

Our simulator is also capable of generating light curves for multi-planetary systems. As of March 2024, out of approximately 5600 stars known to host exoplanets, around 900 have more than one confirmed planet. The stars with the most confirmed planets include our Sun, Kepler-90 (Cabrera et al. 2014), and Trappist-I (Gillon

et al. 2017; Luger et al. 2017). To demonstrate the versatility of our transit simulator, we simulate the transit light curves for the Trappist-I multi-planetary system as described below.

Trappist-I is known to have seven confirmed exoplanets. In order to simulate the light curve for those we run our simulation for one orbital period of the slowest planet, Trappist-Ih. The sizes of the planet and their orbital distance are taken from Gillon et al. (2017). We obtain quadratic limb darkening coefficients for the star from the VizieR Catalog (Ochsenbein F. et. al 2000). For convenience, at the start of the simulation, all planets are assumed to be aligned, and behind the star. The top panel shows a schematic of one frame of the simulation. The sizes of the planets have been scaled up and the distance to each planet has been scaled down in this figure for better visualization. The bottom panel shows the normalized output light curve of this system for one phase duration of the orbit of Trappist-Ih. The noise seen at the bottom of the transit dips is due to Monte-Carlo noise. This example highlights the simulator’s ability to faithfully reproduce the light curves of the intricate multi-planetary systems.

3.3. Tidally Distorted Systems

Tidal effects can cause significant distortions to the shape of the transiting object as well as the host star. Therefore, such systems lead to a variety of non-spherical as well as dynamic shapes which provide excellent grounds for testing the simulator against natural, observable, and already modeled phenomena. In this section, we simulate examples of tidally distorted systems and compare them to existing models.

3.3.1. Tidally Distorted Exoplanet

Giant planets very close to their host stars, such as hot Jupiters, are expected to undergo significant tidal distortions due to the gravitational effects of the star. Most of these systems are tidally locked and hence show a synchronization of their rotation and orbital period resulting in circularization of their orbit. In the absence of such synchronization, orbits can decay because of the angular momentum transfer from orbit to the star, which could eventually result in the planet being engulfed by the star.

The model for tidal distortion developed by Correia (2014) has been utilized to explain peculiar light curve features in many eclipsing binaries. Due to the large size, brightness, and mass, the tidal effects of the companion star on the host star are significant, which adds to the observed unique light curves. The same model can be extended to exoplanets, but in these cases, the tidal distortion signal is weak because of the small size,

little brightness, and low mass of the planet compared to the host star. Moreover, a hot Jupiter is expected to have a negligible effect on the shape of the host star, which makes it more challenging to detect.

Tidal distortion in hot Jupiters has been extensively studied (e.g., Hellard et al. 2019; Kramm et al. 2012). For example, WASP-4 (Harre & Smith 2023) and WASP-12 (Maciejewski et al. 2016) have been found to show a tidal decay. The first tidally distorted system to be observed at a significance level of 3σ is WASP-103b (Barros et al. (2022)). Due to the severity of the tidal effects of this system, it has been observed as a distortion in the shape of the transit. This system has been studied extensively by the Characterizing Exoplanet Satellite (CHEOPS; Benz et al. 2021).

Here, we demonstrate how our simulator can be used to model tidally distorted planets. For that, we choose the example of WASP-103b as a case study. The planet is modeled as a triaxial ellipsoid (see e.g., Correia 2014) with axes r_a, r_b, r_c , where:

$$r_v = \sqrt[3]{r_a r_b r_c}, \quad (8)$$

with,

$$\begin{aligned} r_a &= r_b(1 + 3q), \\ r_c &= r_b(1 - q), \end{aligned} \quad (9)$$

and, the asymmetry parameter q is given by

$$q = \frac{h_f m_p}{2 m_s} \left(\frac{r_b}{r_0} \right)^3. \quad (10)$$

Here, r_v is the mean radius of the triaxial ellipsoid, m_p/m_s represents the mass ratio of the planet to the star, r_0 is the distance between the planet and the star and h_f is the second fluid love number. The second fluid love number is a parameter that describes the rigidity of a body under the effect of gravity. A completely fluid body has an h_f value of 1. Therefore, three parameters are required for fitting: m_p/m_s , r_v , and h_f .

For the demonstration, we choose nine transits of WASP-103b from CHEOPS public data products (program CH_PR100013). To obtain the orbital parameters by fitting this data, we utilize the model *ellc* (Maxted (2016)) which utilizes the model by Correia (2014) to generate a light curve of the system. We use the fitted parameters given in Barros et al. (2022) to generate a model light curve for WASP-103b and compare it to our simulation. The values given in Barros et al. (2022) are $m_p/m_* = 0.001165$, $r_v = 0.1395$ and $h_f = 1.59$.

For our simulation, we use the equations 8, 9, 10 and obtain the values for the three axes of the triaxial ellipsoid for WASP-103b as $r_a = 0.1345$, $r_b = 0.1258$,

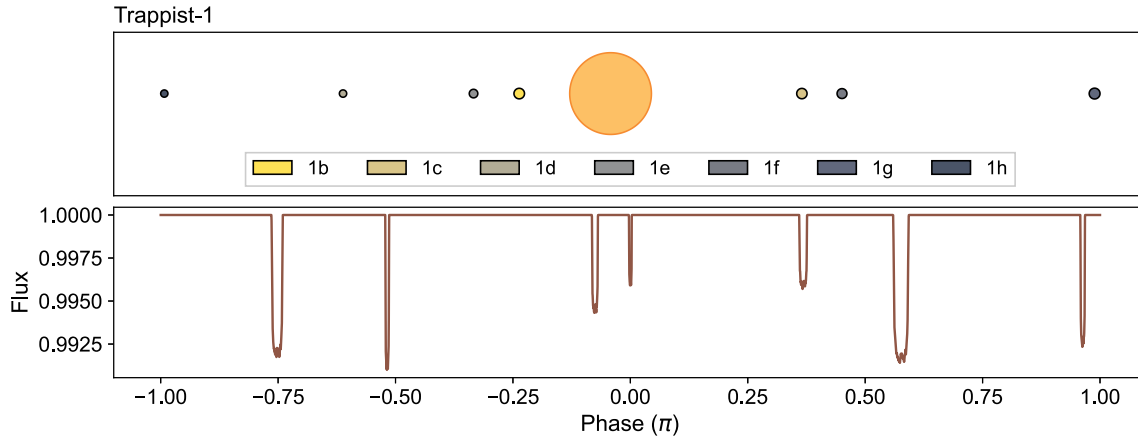


Figure 5. Trappist-1 simulated light curve. The total phase duration is equal to one orbit of Trappist-1h. The top panel shows one frame of the simulation, with the seven planets. The size of the planets has been scaled up and distances have been scaled down for clarity. The planets have been color-coded by their orbital distance. The bottom panel shows the simulated light curve. The simulated light curve is for the realistic system.

$r_c = 0.1605$. We define an ellipsoid planet with these radii and a spherical star with quadratic limb-darkening parameters $u_1 = 0.5269$ and $u_2 = 0.1279$.

The result of our simulation (black lines) is shown in Fig. 6 along with the observations from CHEOPS (gray data points). We find that our simulated light curve agrees closely with the fit provided by *ellc*. The middle panel shows the difference between the observed data and *ellc* fit. In the bottom panel, we show residuals between our model and the *ellc* fits. The residuals in the bottom panel are far less than the residuals of the fit in the middle panel, which shows that our model is in excellent agreement to the data. The bottom panel residuals are of the order of 50 ppm which is mainly because of the Monte Carlo noise.

This exercise demonstrates that our transit simulator is capable of reliably and accurately modeling the light curves of tidally distorted planets. In the subsequent subsection, we apply our simulator to to model tidal distortions in highly eccentric eclipsing binaries known as heartbeat stars.

3.3.2. Heartbeat Stars

Heartbeat stars, a class of eclipsing binary stars orbiting in highly eccentric paths, represent unique astrophysical systems where the eccentricity of their orbits induces significant distortions in their light curves. When the stars are at their closest approach, the proximity leads to tidal distortions and pulsations, causing the characteristic heartbeat shape of their light curves. A large number of heartbeat starlight curves have been identified by *Kepler* (e.g., Hambleton et al. 2018, 2016) and *TESS* (e.g., Kołaczek-Szymański et al. 2021).

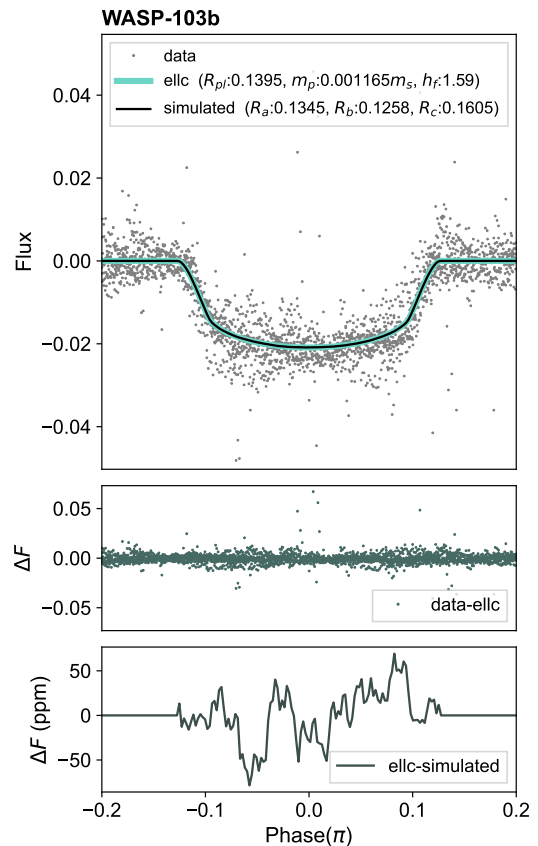


Figure 6. Simulated light curves for WASP-103b. The top panel shows phase folded transits from CHEOPS (gray), the *ellc* light curve with appropriate parameters, and the simulated light curve. The middle panel shows the residuals from the observation (data-*ellc*), whereas the last panel shows the residuals between the simulation and *ellc*.

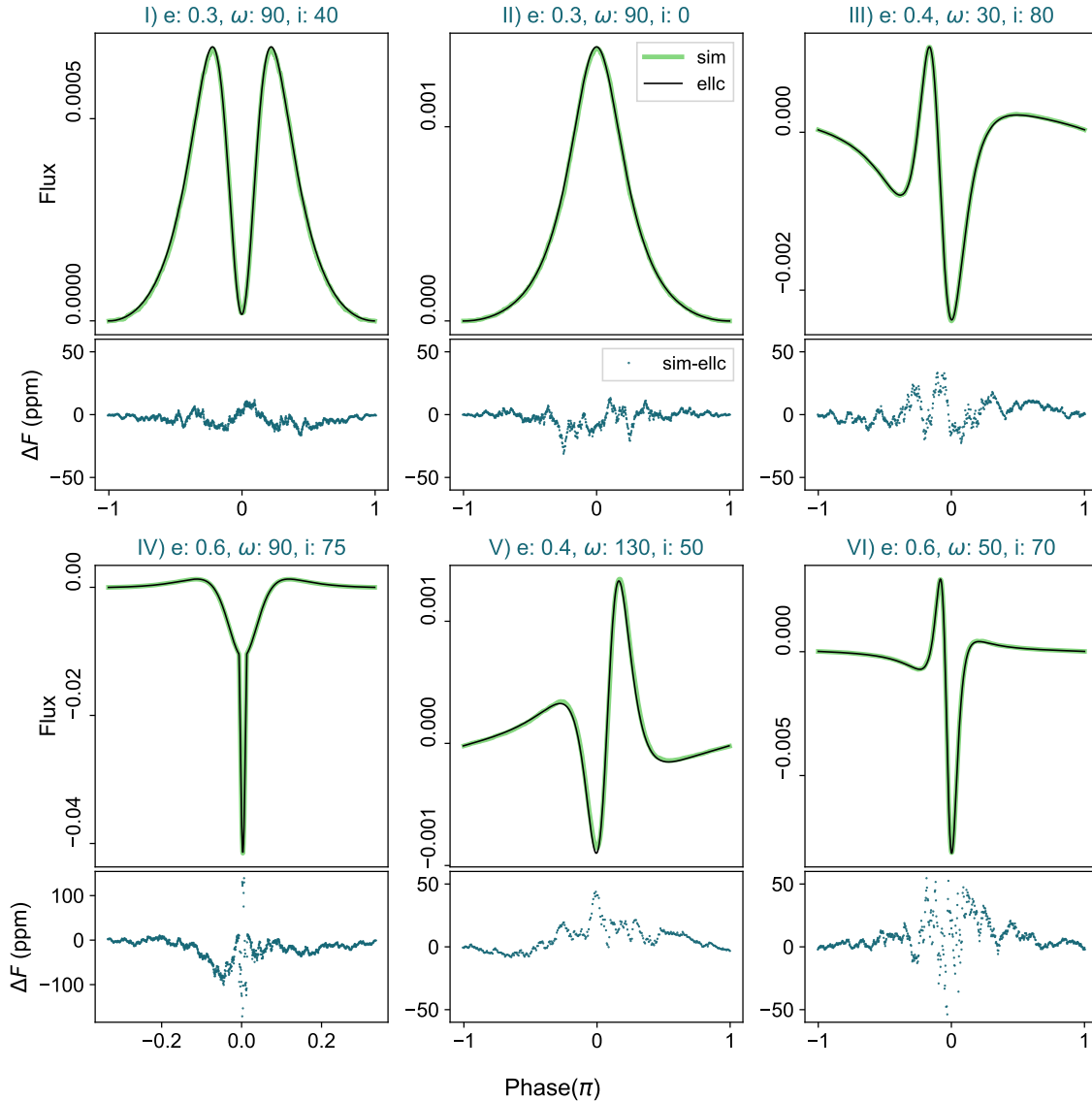


Figure 7. Simulated heartbeat star systems in various configurations. Each panel is a configuration with a value of e, ω, i . The radius-ratio ($r_s/r_p = 0.5$), semi-major axis ($12.5r_p$), fluid love number (1.5) and mass ratio ($m_s/m_p = 0.9$) is the same for all the configurations. The top panels plot the simulation (green) and the *ellc* model (black). The bottom panels plot the residuals.

The shape of the heartbeat system light curve can vary widely. It depends primarily on three parameters, the eccentricity of the orbit (e), the longitude of periastron (ω), and the inclination of the orbit (i). The top panels of Fig. 7 show some of these configurations.

We simulate the heartbeat systems using an ellipsoidal star with a spherical companion. For our simulations, the companion is assumed to have negligible brightness compared to the star. The companion causes tidal distortions in the primary star, which causes the variability in observed flux. This may or may not be accompanied by a transit. From the tidal equations defined in Eq. 10, the asymmetry parameter q depends on the distance to the center of the star. We evaluate this distance for

each point in the trajectory, which gives us values of r_a, r_b , and r_c (see Eq. 8, 9) for the ellipsoidal star (for illustration see the last panel in Fig. 2 I). We choose an h_f value of 1.5 for the primary star. The size ratio (r_s/r_p) of secondary to primary is taken as 0.5, and the semi-major axis is taken as $12.5r_p$. The mass ratio of secondary to primary is 0.9 (m_s/m_p). Similar to the model *ellc*, we also assume a synchronous rotation of the primary star, tidally locked to the secondary star. In reality, these systems do not exhibit perfect synchronous rotation.

The top panels of Fig. 7 show the simulated light curves of a heartbeat system in six different configurations. For comparison, we also generate a heartbeat

light curve using the *ellc* model with the same parameters mentioned above and show those in Fig. 7. In the bottom panels, we show the difference between our model and model *ellc* which are of the order of ppm and results of the Monte-Carlo noise. Some of the residuals in the bottom panels show fluctuations (see Fig. 7 IV, VI). These are due to narrow features with sharp transitions in the light curve indicating that we need more frame resolution to reduce the noise. Nevertheless, this exercise demonstrates that our simulator can be used to accurately model complex light curves of tidally distorted stars such as heartbeat systems. It emphasizes that our simulator can adeptly handle various intricate scenarios. Moving forward, in the next subsection we will simulate the light curves of a known exocomet candidate.

3.4. Exocomets

The discovery of exocomets around β -Pictoris (Ferlet et al. 1987) predates the discovery of exoplanets. With the launch of *TESS* this comet system has been studied in extensive detail. Extensive modeling of an exocomet transit has been done by Lecavelier Des Etangs et al. (1996) and Brogi et al. (2012b). These models along with *TESS* data have been used to study the β -Pictoris system in great detail. This has also prompted the search for exocomet transits in existing Kepler light curves.

In this work we adapt the model of Rappaport et al. (2018) which has been used to find exocomet candidates in the star KIC 3542116 and KIC 11084707. In this work, the exocomet in the star KIC 3542116 has been modeled as an occulter with sustained dust outflows. Because comets are expected to be in highly eccentric orbits, the orbital period of the comet is assumed to be much larger than the transit duration. Hence, the transverse velocity v_t is assumed to be constant during the transit. The dust tail is also assumed to be narrow, and its extinction follows an exponential decay profile with the distance from the comet. The profile of the dust tail is given as:

$$\tau = Ce^{-\frac{x-x_c}{\lambda}} \quad x < x_c; y - y_c < \Delta b/2 \quad (11)$$

Here, τ is the optical depth of the comet dust tail, C is a normalization constant, λ is the decay parameter for the optical depth, x is the x -coordinate of a point on the stellar projection on the sky plane and x_c is the x -coordinate of the center of the comet nucleus. The width of the comet and the dust tail perpendicular to its velocity is given as Δb which is assumed to be negligible as compared to R_{st} and therefore is degenerate with the normalization constant C . Therefore the comet is

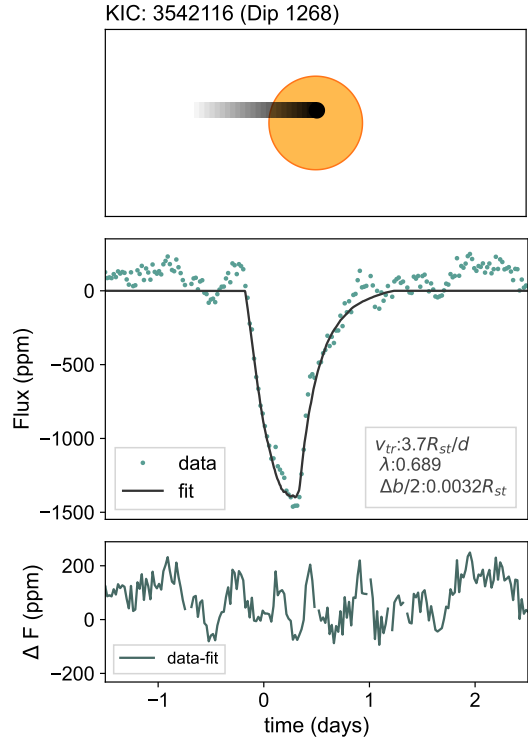


Figure 8. Exocomet simulation for candidate KIC: 3542116 Dip 1268. The top panel shows a schematic of the simulation geometry. The comet size has been exaggerated for visual clarity. The middle panel shows the light curve of KIC 3542116 and the simulated comet model. The bottom panel shows the residuals (data - simulation). The fitted parameters are given.

modeled as six free parameters, $t_0, \lambda, C, v_t, b, DC$, where b is the impact parameter of the transit, and DC is the background flux level away from the transit.

For our simulation, we take a spherical nucleus and a dust tail of the comet to be of the same width. For the dust tail, we model an elongated rectangular shape with exponentially decreasing opacity. We take the normalization constant as 1 and instead take the size of the comet system as a free parameter. Since any eccentricity information is unavailable, we assume this shape to be in a circular orbit around the star. The simulation agrees with the analytical model within the transit duration, but this assumption will not be valid out of transit. The schematic of our simulation geometry is shown in the top panel of Fig. 8. The simulation requires the free parameters: $R_{orb}, R_{comet}, \lambda, b, t_0$.

We simulate the light curve of one of the observed dips in the system KIC 3542116, which is observed at day $t_0 = 1268$. The impact parameter value is 0.27 and is taken from the parameter obtained by Rappaport et al. (2018). We use $u_1 = 0.2736$ and $u_2 = 0.3001$

as the quadratic limb darkening coefficients (see Eq. 1) from the VizieR Catalog (Ochsenbein F. et. al 2000) given for this star. Since our simulation gives the output flux in terms of the phase instead of time, we choose $\Delta\theta = \Delta t(\text{days})$, i.e. one orbital period as 2π days, which gives us,

$$v_t = R_{orb}(R_{st}/\text{day}).$$

The normalized light curve from Kepler data and the simulated light curve are shown in the middle panel of Fig. 8. We see that the simulation is in close agreement with the data. This is also visually similar to the fit demonstrated in Figure 3 of Rappaport et al. (2018). We obtain a simulated value of $v_t = 3.7R_{st}/\text{day}$ and $\lambda = 0.689$, which is close to the values mentioned in Table 2 of Rappaport et al. (2018). We also obtain $R_{comet} = 0.0032R_{st}$. The bottom panels of Fig. 8 show the residuals of the fit, which is significantly lower than the noise in the transit light curves particularly away from the transit dip. This exercise highlights that our simulator can be used to model the exocomet light curves reliably. Moreover, the agreement between our simple visual good-fit and the parameters obtained by Rappaport et al. (2018) shows that our simulator can be reliably used to infer the physical parameter of the observed exocomet light curve.

4. TRANSITING MEGASTRUCTURES: DYSON SWARM, RINGS AND DISCS

Building on this algorithm, we have extended the use of our simulator to investigate potential indicators of advanced alien civilizations through the transit of massive megastructures. Envisioned as creations of extraterrestrial societies to collect energy from their stars, these vast constructs are expected to produce distinctive patterns in the light curves. In the next subsection, we illustrate our simulator’s capability to accurately model the light curves of a range of megastructures, with a specific focus on Dyson Swarm, Dyson Ring, and Dyson Disk - a circular opaque disk rotating around the host star - as prime examples.

4.1. Dyson Swarm

The main example of a megastructure that can be built by a type 2 advanced civilization (Kardashev 1964) is a Dyson sphere (Dyson 1960). However, such a rigid structure as envisioned originally is not stable and instead one needs a collection of individual smaller structures, which is called a Dyson Swarm (Smith 2022). For the Dyson swarm, one can imagine co-rotating solar panels in orbit around stars in such a way that they harness the energy of the host star. In order to simulate a Dyson Swarm in the process of building, we assemble large solar

panels, one at a time, and allow them to revolve around a star. We can add more solar panels near the previous panels in such a way that eventually the whole area around the host star gets covered. One such incomplete structure is shown in the left-hand panel of Fig. 9.

We use this incomplete Dyson Swarm configuration in our transit simulator and obtain the light curve for it assuming it revolves around the star. In this Dyson Swarm, the orbit of the equatorial panels is at a distance $2R_{st}$ from the center of the star where R_{st} denotes the radius of the star. To ensure seamless coverage around the circumference of the orbit, the size of each panel has been carefully calculated to allow for an exact integer number of panels to fit. Specifically in this example, the orbit’s circumference is fully covered by 40 panels, each having a size of $0.157R_{st}$ for the equatorial panels. For panels situated away from the equator, their orbital positioning is determined based on their latitude ϕ , with orbits set at distances of $2\cos\phi R_{st}$ from the star. This arrangement ensures that, regardless of latitude, the same number of panels (i.e. 40) can be uniformly distributed around the circumference of each orbit. The simulation, depicted in Fig. 9, incorporates a total of 100 panels. The resulting light curve, presented in the bottom left panel of the figure, exhibits a significant transit dip due to the extensive coverage of the panels. Despite this coverage, there remain inter-panel gaps that allow light to pass through. As this incomplete Dyson sphere configuration orbits the star, the varying positions of these gaps and panels relative to the observer’s line of sight produce the observable undulations seen in the transit light curve (see Fig. 9).

In fact, the structure itself lacks stability in this configuration. It is assumed that panels rotate coherently along identical latitudinal lines which is an unstable Keplerian orbit except at $\phi = 0$. However, this configuration was designed to demonstrate the versatility of our simulator in predicting light curves for any arbitrary configuration orbiting stars. In the next subsection, we turn our attention to a more stable construct: the Dyson ring. This structure comprises a singular ring of solar panels that rotates in unison around the host star.

4.2. Dyson Ring

To assemble a complete Dyson sphere, advanced civilizations might construct a series of rings around their stars. These rings, made up of numerous small panels, would rotate in Keplerian orbits to maintain stability. By strategically arranging these rings at different orientations, they could comprehensively encircle the star. Each ring would orbit at a slightly different distance from the star to prevent any overlap or collisions.

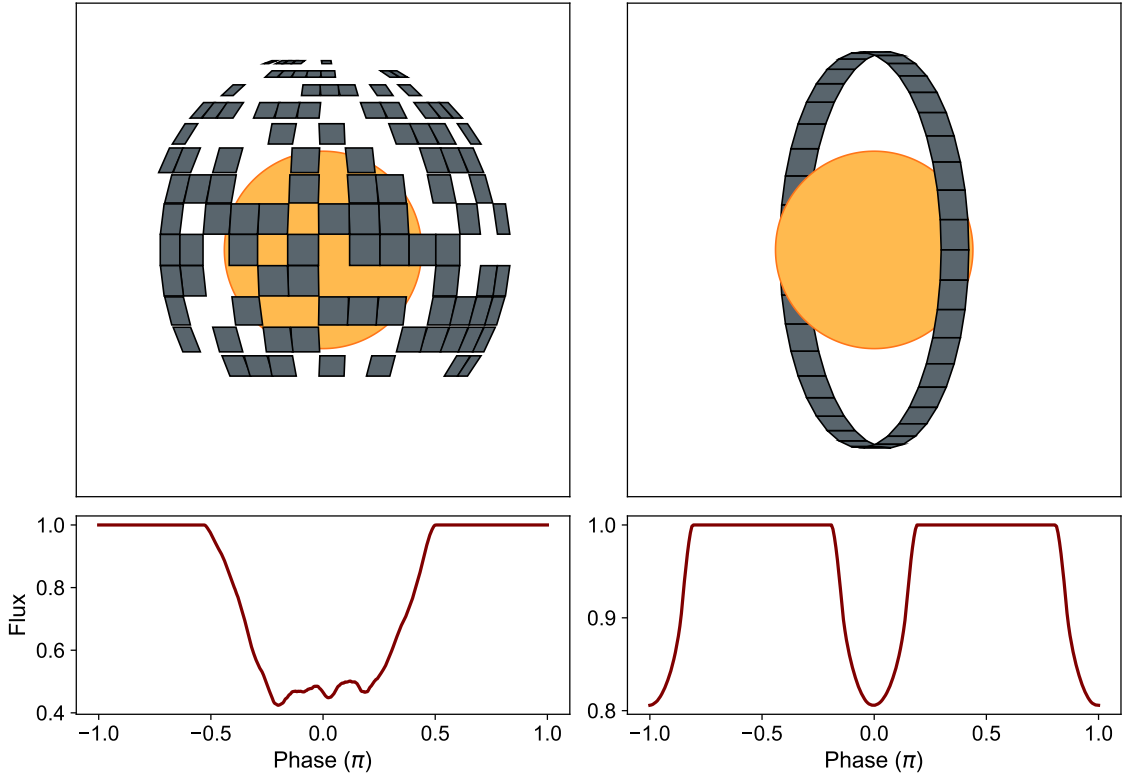


Figure 9. Transit of weird objects. The right panel imagines a Dyson sphere in partial construction, causing gaps between the Dyson disks. The size of individual panels is $0.157R_{st}$ at a distance of $2R_{st}$ which corresponds to 40 panels at the equatorial circumference. Away from the equator, the orbits and sizes are scaled according to the latitude, in order to maintain 40 panels in any circumference. A total of 100 panels are placed in this incomplete Dyson swarm. The bottom-left panel shows the resulting transit light curve, which shows a highly asymmetric and distorted geometry. The left panel shows a transit of a hypothetical polar ring. The ring is made of 41 panels, each of size $0.153R_{st}$ at a distance of $2R_{st}$. The bottom-right panel shows the resulting transit, which is very similar to a planet transit with half the orbital period.

Illustrating this concept, we present a simulation of a polar ring composed of solar panels around a star, as shown in the right panel of Figure 9. We chose an example of a polar ring because a complete ring at the equator would not lead to a transit effect. This is because an equatorial ring will block the same portion of the starlight all the time leading to no differential change in the light curve.

For the polar ring shown in Fig. 9 (top panel), we assembled 41 square panels of the size $0.153R_{st}$ orbiting at a distance of $2R_{st}$ from the star. The resulting light curve, displayed in the bottom right of Fig. 9, is akin to the light curve from a planet transit, however, it occurs over half the orbital period.

4.3. Dyson Disk

Transitioning from our investigation of Dyson swarms and rings, we explore a notable megastructure concept: a large solar panel in orbit, designed to constantly face the star for optimal energy collection. This raises the question: if this panel is circular and the size of a typ-

ical planet or larger, how does its transit light curve differ from that of a planet? We name such a panel as a Dyson disk. In addition to studying the light curve of the Dyson disks, in this subsection, we investigate the challenges associated with detecting those within the extensive dataset of the Kepler mission.

4.3.1. Transit of a Dyson disk

We expect the transiting Dyson disk will produce distinct signatures on the light curve, differing from those of a planet. It is because the projection of a planet on the sky plane is always a circle whereas the projection of the Dyson disk would be mostly elliptical except at the midpoint of the transit. This is depicted in the top panel of Fig. 10. The requirement for Dyson disks to always face the star causes them to rotate, resulting in their predominantly elliptical projection on the sky plane. We illustrate the transit light curves for a Dyson disk, in the bottom panel of Fig. 10, orbiting at the equator of a star (i.e., with an impact parameter of zero) at a distance of $2R_{st}$ and with a size of $0.3R_{st}$.

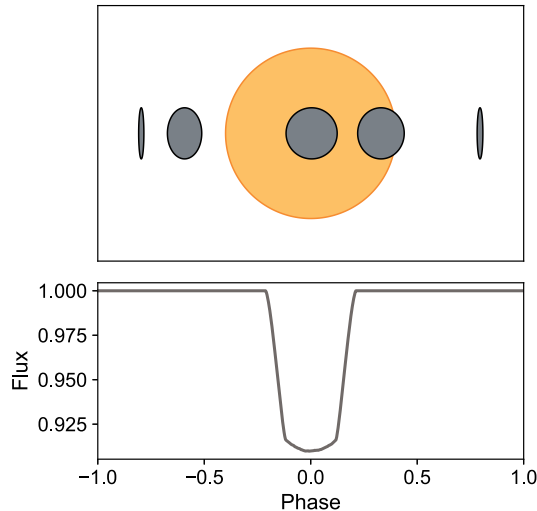


Figure 10. A schematic showing the orbital configuration of a Dyson disk. The top panel shows five orientations of a flat circular 2D structure along the orbit. The size of the structure is $0.3R_{st}$ at a distance of $2R_{st}$. The bottom panel shows the resulting transit.

For comparison, four panels in Fig. 11 show light curves generated for Dyson disks (at distance $2R_{st}$, size of $0.3R_{st}$ and $b = 0$) for two different limb-darkening coefficients and two distinct eccentricities. Each panel also includes the light curve of a planet with identical radius and orbital parameters as the Dyson disk as well as the host star. In panel (A), we display the Dyson disk’s transit around the star in a circular orbit (i.e. with $e = 0$) without limb darkening. The lower segment of the transit reveals a curvature due to the gradual change in the area of the projected ellipse onto the star, contrasting with the planet’s flat-bottomed light curve.

In the bottom part of the panel (A) of Fig. 11, we show the differences between the Dyson disk and the planet’s light curves by subtracting the Dyson disk’s light curve from the planet’s. Notable features emerge in this comparison. Initially, the Dyson disk’s entry is slightly delayed because of its rotation to maintain a star-facing orientation, resulting in a sharp increase in the difference. As the Dyson disk enters the transit it starts to block the starlight, this modifies the slope of the difference in the light curve. A slight kink in the difference curve, preceding the slope change, marks the beginning of the Dyson disk’s ingress. During the ingress phase, the planet obscures more light than the Dyson disk, causing the difference to increase. Once the planet completes its ingress, the amount of light it blocks remains constant, while the Dyson disk continues to gradually increase its blockage. This reduces the difference in the light curves until the Dyson disk reaches the star’s

center, where its projection becomes a circle of the same size as the planet’s projection, and both block an equal amount of radiation, nullifying the light curve difference at the transit’s midpoint. Due to the symmetry of the situation, the pattern observed is mirrored until both the planet and Dyson disk exit the transit.

The observed patterns in the light curves and their differences persist for orbits around the star when realistic limb darkening is considered as shown in panel (B). However, the magnitude of these differences is slightly diminished due to the limb-darkening effect, which dilutes the sharp transitions seen during ingress and egress because of otherwise uniformly bright edges.

Interestingly, in a specific setup within an eccentric orbit—where the periapsis is aligned perpendicular to the line of sight—the light curves for both the planet and Dyson disks display asymmetry, as demonstrated in panels (C) and (D) of Fig. 11. This asymmetry primarily arises because both objects linger longer in the transit phase during egress. Furthermore, this discrepancy in the light curves is more pronounced on the asymmetric edge for the Dyson disk which is evident more clearly in the bottom panels where the difference pattern is also asymmetric, with one side showing a larger difference than the other.

In order to detect these Dyson disks, one can estimate a crude signal-to-noise ratio (SNR) required in the transit data for determining the peaks in the residual features shown in the bottom panels of Fig. 11. The SNR of a transit is defined as the ratio of the transit depth to the noise of the signal. For example, in order to get the optimal signal-to-noise ratio, we choose the transit shown in the second column of Fig. 11, which has the shortest residual peak. For this, the transit depth is 1.158×10^{-2} , and the peak of the residual is at 9.323×10^{-4} .

Therefore to detect this peak in the residual at a significance level of 3σ , we need an SNR of 37. This is consistent with many of the transits observed by the *Kepler Space Telescope*, where 35% of the detected Kepler Objects of interest have transits with SNR greater than 37 (NASA exoplanet science institute 2010). However, the number estimated here is only applicable to a simulation of a Dyson disk with fixed parameters. In the following subsection, we explore what are the favourable conditions on the Dyson disk parameters that can increase the chances of their detection.

4.3.2. Viability of Detection

In order to examine the viability of the detection of Dyson disks, we first need to characterize the variation of the residual feature, i.e., the difference between the

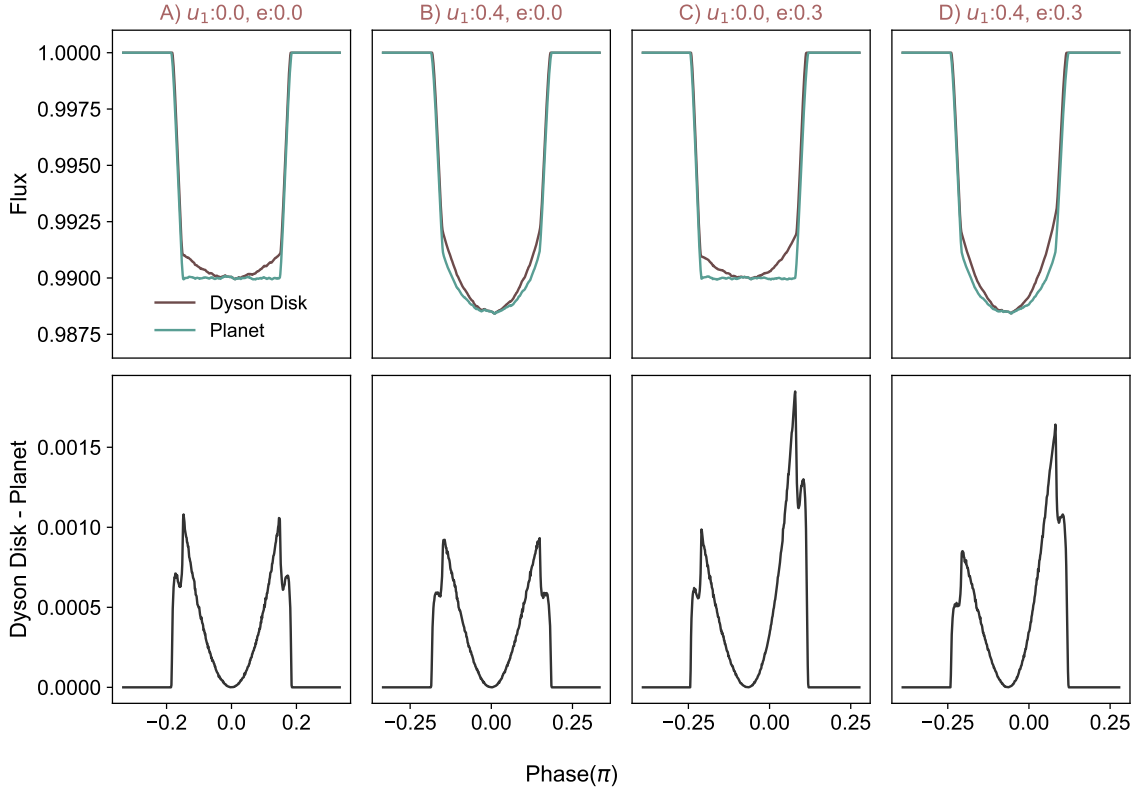


Figure 11. Transit of a Dyson disk, compared to the transit of a planet of the same dimensions and distance to the star. The top panel shows the lightcurves obtained for a planet as well as Dyson disk transits. All the systems have a size $R_{pl} = 0.1R_{st}$ and $R_{orb} = 2R_{st}$. The bottom panel shows the residuals (Dyson Disk - Planet transit). Column A shows a simple transit with no eccentricity or limb darkening. While the planet transit is flat, the Dyson Disk transit shows an upward curvature during ingress and egress due to the change in the projection area. Column B adds limb darkening to the first transit which diminishes the residual feature. Column C shows a transit with an eccentric orbit with the semi-major axis perpendicular to the line of sight. The Dyson Disk light curve shows significant asymmetry in ingress and egress due to the change of area of projection. Column D shows the same system with limb darkening. This results in a slightly diminished, but still significant residual feature.

transit of a Dyson disk and a planet with the same size and orbital parameter (as shown in the bottom panels of Fig. 11). We investigate these residuals for Dyson disk and planets with different transit parameters. For this, we generate simulated light curves of a Dyson disk and a planet for a range of transit parameters and calculate the residuals. Fig. 12 depicts the variation of the residual features across four parameters – the R_{pl}/R_{st} , ratio of the orbital radius R_{orb}/R_{st} , limb darkening parameter u_1 and the impact parameter b . The top panels show the different residual features. The color bars are indicative of the values of the transit parameters. For each simulated set, we find the maximum deviation in the residuals by calculating the magnitude of the peak of the residual feature (ΔF_m). The bottom panels of Fig. 12 show the ΔF_m with the variation of the respective transit parameter.

Fig. 12 panel (A) shows the variation of residuals with R_{pl}/R_{st} . In figure the R_{orb}/R_{st} is fixed at 2.0 whereas

u_1, u_2 and b are kept at 0. We can see that the ΔF_m value increases with the radius of the planet, especially in the regime of $R_{pl} > 0.1R_{st}$. This is expected, since the bigger the object, the more significant the distortion should be. Fig. 12 panel (B) shows the variation of residuals with R_{orb}/R_{st} . Here the R_{pl}/R_{st} is kept at 0.2 whereas u_1, u_2 and b are at 0. We see that ΔF_m increases with decreasing radius of orbit. The distortion is significant for radii smaller than $10R_{st}$. This is because, due to a greater transit duration relative to the orbital period, the projection of a Dyson disk that is close to the star would have a large variation in the area of the projected elliptical shape during the transit duration, leading to greater differences in the residuals.

Fig. 12 panel (C) shows the variation of residuals with limb darkening parameter u_1 . Here R_{orb}/R_{st} is kept at 2, R_{pl}/R_{st} at 0.2 and b as 0. We observe that ΔF_m decreases linearly with an increase in the limb darkening parameter, which means that the chances of detection

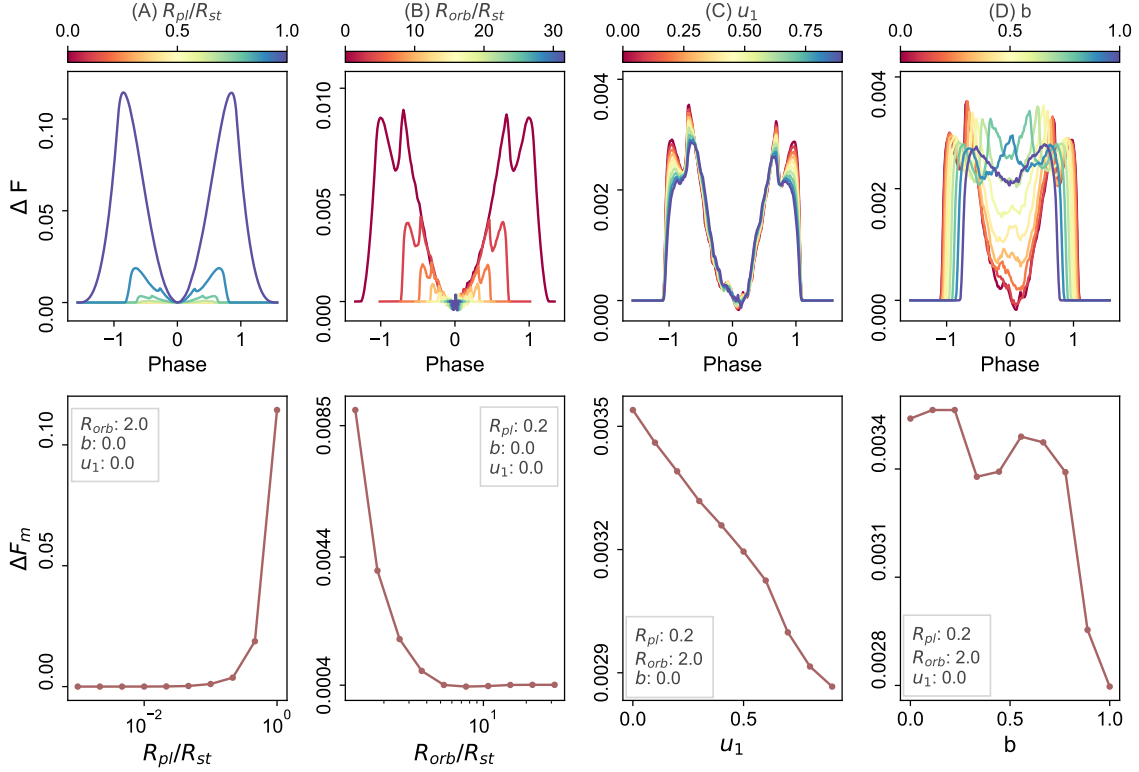


Figure 12. Evolution of the residual feature obtained by Dyson Disk transit minus planet transit with transit parameters. Column (A) is for R_{pl}/R_{st} . The top panel shows the residuals for different values of R_{pl}/R_{st} , which are represented by the color-map. The bottom panel shows the variation of ΔF_m with R_{pl}/R_{st} . ΔF_m is the maximum difference observed between the Dyson disk and planet light curve. There is a sharp increase in ΔF_m for values greater than 0.1, which implies greater detectability. Column (B) is for R_{orb}/R_{st} . Once again, a sharp increase is observed for orbits closer than $10R_{st}$. Column (C) is for u_1 . There is a linear decrease in ΔF_m . Column (D) is for b . There is an overall decrease in ΔF_m , however, the shapes of the residuals vary significantly, as is observed in the top panel.

of such a feature may be better for stars with smaller limb darkening coefficients. As explained before, this is because the fainter edges of the stars dilute the contrast between the planet and the Dyson disk arising from the projection effect during ingress and egress.

Fig. 12 panel (D) shows the variation of residuals with impact parameter. Similar to previous case, here R_{orb}/R_{st} is kept at 2, R_{pl}/R_{st} at 0.2 along with both u_1 and u_2 at 0. We see an overall decline of ΔF_m with the impact parameter. However, this is more complex, because the shape of the residuals changes with impact parameter. At a higher inclination, the object never attains a full circular projection, causing a reduction in the transit depth, which is why the deviation at phase 0 increases with b . However, the phase at which ingress occurs also reduces at high inclinations, leading to a lesser curved shape at ingress. This causes the sharp peak at the edges of the residuals to decline at high inclinations.

From this analysis, we infer that the probability of observing deviations from typical transit signatures is

greater for transits of Dyson disks that are large and revolving close to the star. To identify such features within existing datasets, targeting transits with $R_{pl} > 0.1R_{st}$ and $R_{orb} < 10R_{st}$ would provide the highest chance of detection. Furthermore, focusing on transits characterized by low orbital inclinations and minimal limb darkening coefficients will improve detection capabilities.

4.3.3. Degeneracies in Detections

The main challenge for finding megastructures such as the Dyson disk is to obtain an unambiguous detection. Specifically, for the Dyson disk, we investigate the potential for its transit signature to be indistinguishable from other natural phenomena.

Qualitatively, the transit of the Dyson disk appears quite similar to that of a planet, particularly due to the additional curvature at the bottom, which resembles a planet orbiting a star with pronounced limb darkening. Consequently, it seems reasonable to attempt fitting a transit light curve model of a planet to the transit of a Dyson disk. If limb darkening coefficients are consid-

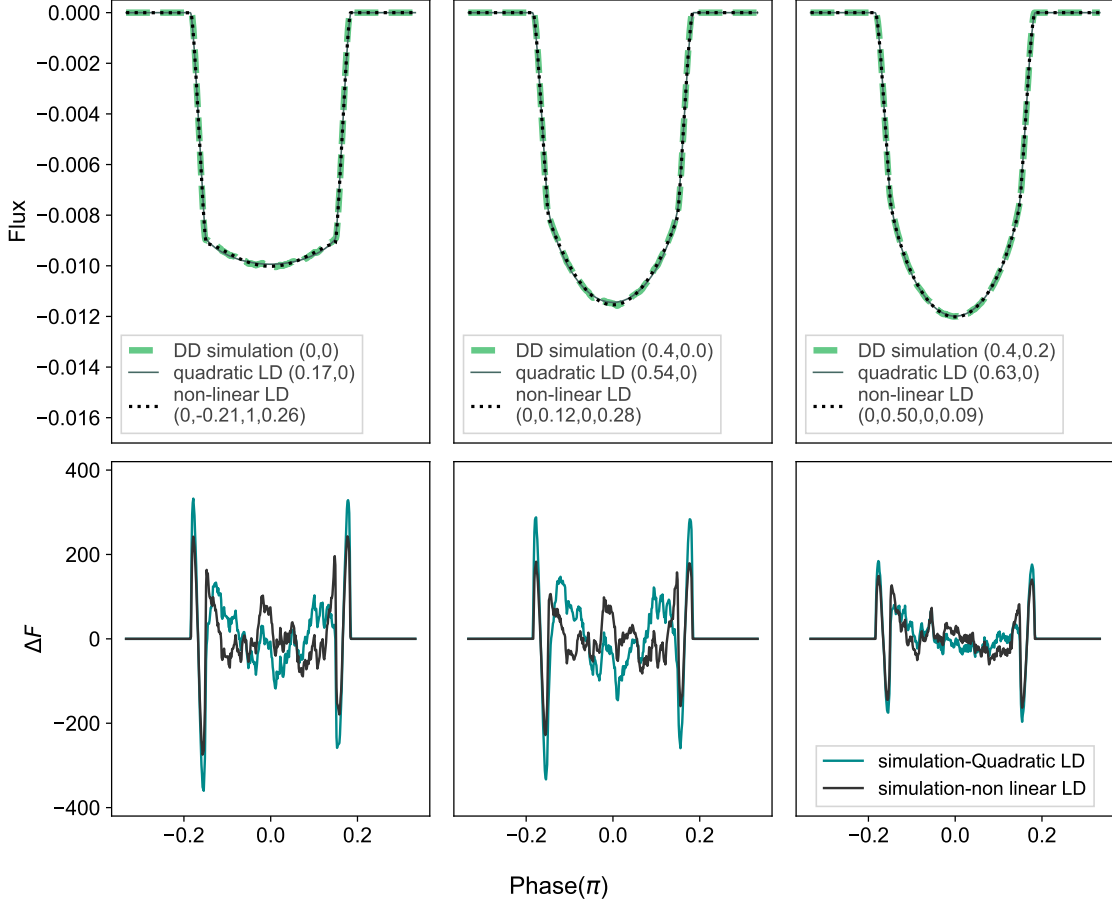


Figure 13. Three simulated Dyson disk light curves with different limb-darkening parameters fitted with exoplanet models. The radius ($0.1R_{st}$), orbit ($2R_{st}$), and impact parameters ($b = 0$) are kept the same for all three examples. A 3D planet model with both quadratic as well as non-linear limb darkening is fit to the Dyson Disk simulations. The top panels show the simulated light curves (green) and the fitted models. The bottom panels show the residual features (Simulation - Fit). The limb darkening coefficients for the simulated Dyson disk light curve as well as the planet fits are mentioned. From the residuals of the non-linear fit (purple) and that of the quadratic fit (blue), The non-linear law appears to fit slightly better than the quadratic law. Such a fit diminishes the residual feature, but kinks are observed at ingress and egress.

ered variable parameters (Espinoza & Jordán 2016), in the absence of other independent measurements, fitting a planetary transit to the Dyson disk might result in higher limb darkening coefficients. On the other hand, since the Dyson disk enters late in the transit reducing the transit duration will result in a fitted planet of a slightly smaller size and larger orbital radius than the Dyson disk. In this analysis, we explore the accuracy with which a planetary transit can be fit to the transit of the Dyson disk and whether there are distinct features in the fit capable of differentiating between the transit of the planet and a Dyson disk.

In Fig. 13, we simulate Dyson disks of size $0.1R_{st}$ at an orbital distance of $2R_{st}$ with an impact parameter of zero for the stars with three limb darkening models. The first model (*left panel*) is without limb darkening and the second model (*middle panel*) and the third model (*right*

panel) have different quadratic limb darkening coefficients namely $u_1 = 0.4, u_2 = 0.0$ for the middle panel and $u_1 = 0.4, u_2 = 0.2$ for the last panel. To these three models, we fit two models of planet light curves; one with quadratic limb darkening law (Eq. 1) while the other with a non-linear limb darkening law (Eq. 2). We use a simple curve-fitting tool provided in Python library `scipy` which uses the non-linear least squares method to fit parameters: R_{pl}, R_{orb}, b, u_1 and u_2 .

As expected, the planetary transit fits give large limb darkening values, slightly smaller size (R_{pl}), and larger orbital radius R_{orb} . For example, as shown in the left panel of Fig. 13, for the model with both limb darkening coefficients set to zero, the best-fit planet transit model with quadratic (non-linear) limb darkening law provides $u_1 = 0.17$ while u_2 remains zero. This is accompanied by $R_{pl} = 0.0968$ and $R_{orb} = 2.009$. Whereas for the

fit with the non-linear limb darkening model, our fits determine coefficients $(a, b, c, d) = (0.0, -0.21, 1.0, 0.26)$ along with $R_{pl} = 0.0971, R_{orb} = 2.009$.

A similar pattern of obtaining higher limb darkening coefficients is seen in the middle and right panels of Fig. 13. For example, the middle panel contains a simulated light curve of the Dyson disk with $(u_1, u_2) = (0.4, 0)$ which is interpreted in the planet fit as $(u_1, u_2) = (0.54, 0)$ and $(R_{pl}, R_{orb}) = (0.0968, 1.997)$. The non linear limb darkening fit gives coefficients $(a, b, c, d) = (0.0, 0.12, 0.0, 0.28)$ and $(R_{pl}, R_{orb}) = (0.0974, 2.011)$. Whereas the third panel contains a simulated light curve of Dyson disk with $(u_1, u_2) = (0.4, 0.2)$ which is interpreted in the planet fit as $(u_1, u_2) = (0.63, 0)$, $(R_{pl}, R_{orb}) = (0.0973, 2.006)$ using quadratic law and $(a, b, c, d) = (0.0, 0.50, 0.0, 0.86)$, $(R_{pl}, R_{orb}) = (0.0975, 2.012)$ using non-linear limb darkening law.

Even though the Dyson disk appears to be degenerate with the limb darkening, it was ineffective in eliminating the residual features entirely. It introduces kinks in the ingress and egress potentially because of trying to optimize for the size of the planet, orbital radius, and limb darkening to fit most of the transit. Using a higher-order or non-linear limb darkening law does improve the fit slightly but is not significant enough and still gives the same features in the residuals.

It is worth noting that when we fit the planet's transit to a model transit of a Dyson disk, not only do the residuals look different, but the value of peaks in the residuals also decreases. For example in the third panel of Fig. 11, the peak of residuals is at 9.32×10^{-4} which is reduced by almost a factor of three (i.e 2.81×10^{-4}) when we fit the planet's transit in the middle panel of Fig. 13. Therefore this time we need a SNR of 123, three times higher than what we estimated in Sec. 4.3.1, for detecting such a signal in the residuals with a significance level of 3σ .

Other degeneracies could arise from natural phenomena such as tidal distortion of planets, gravity-darkening, and star spots, which might be mistaken for Dyson disks. We aim to thoroughly investigate these degeneracies in our future research as we search for Dyson disk candidates in Kepler and TESS datasets (Bhowmick et al. in prep.).

5. CONCLUSION

We have developed a numerical transit simulator designed to generate light curves for objects of any arbitrary shape transiting stars. This simulator employs a simple Monte-Carlo technique to compute accurate light curves, incorporating realistic limb-darkening profiles and geometries of stars. Throughout this article, we

have demonstrated the broad applicability of the simulator to a variety of both natural and artificial structures in stellar orbits.

We demonstrate that our transit simulator accurately models the transits of single planets (Fig. 3) and multi-planetary systems such as Trappist-I (Fig. 5). Additionally, it can model the transits of tidally distorted binary stars and giant planets (see Fig. 6 and 7). Furthermore, we illustrate its capability to simulate transits of exocomets, using the example of a Kepler exocomet candidate (KIC 3452116, Fig. 8). These examples collectively highlight the versatility of our simulator in generating light curves for a diverse range of natural transits.

We show that our simulator is capable of generating transit light curves for artificial structures, such as those that might be constructed by Type I to Type II advanced civilizations, with examples including a Dyson swarm and a Dyson ring (Fig. 9). Additionally, we introduce a new structure that we name a Dyson disk: a large circular disk that rotates around a star while maintaining constant orientation towards it. Dyson disk can be thought of as a building block of a Dyson swarm. We explore how the transit light curve of a Dyson disk can be distinguished from that of a planet and discuss potential ambiguities due to limb darkening (Sec. 4.3). Furthermore, we provide a preliminary assessment of the signal-to-noise ratio required in the light curve to identify candidates for such Dyson disks. We will explore such Dyson disk candidates and potential degeneracy with other natural phenomena in the upcoming articles (Bhowmick et al. in prep.).

In conclusion, the versatility of our numerical transit simulator will prove invaluable for understanding a wide array of transit phenomena involving both natural and artificial structures. We will make this code available to researchers to facilitate the study of various natural transits and support the ongoing search for technosignatures, thereby aiding in the broader quest to detect signs of advanced civilizations.

This research has made use of the NASA Exoplanet Archive, which is operated by the California Institute of Technology, under contract with the National Aeronautics and Space Administration under the Exoplanet Exploration Program. This paper includes data collected by the Kepler mission and obtained from the MAST data archive at the Space Telescope Science Institute (STScI). STScI is operated by the Association of Universities for Research in Astronomy, Inc., under NASA contract NAS 5–26555. This paper also uses data from the program CH_PR100013, which is a part of the public release of the WASP data as provided by the WASP consortium and services at the NASA Exoplanet Archive. For the various limb darkening coefficients, this work has made use of the VizieR catalog access tool, CDS, Strasbourg, France.

Dr. Vikram Khaire acknowledges support for this work through the INSPIRE Faculty Award (No. DST/INSPIRE/04/2019/001580) of the Department of Science and Technology (DST), India. Ushasi Bhowmick thanks the Astronomy and Astrophysics Department, Indian Institute of Space Science and Technology for their extensive review of this research work, as well as Dr. A. S. Arya (SAC), Dr. Mehul R. Pandya (SAC), Dr. Rashmi Sharma (SAC) and Director SAC for their support. We thank Nick Tusay for suggesting the megastar name ‘Dyson disk’ discussed in Section 4.3.

REFERENCES

- Albrecht, S., Winn, J. N., Johnson, J. A., et al. 2012, *ApJ*, 757, 18, doi: [10.1088/0004-637X/757/1/18](https://doi.org/10.1088/0004-637X/757/1/18)
- Arkhypov, O. V., Khodachenko, M. L., & Hanslmeier, A. 2021, *A&A*, 646, A136, doi: [10.1051/0004-6361/202039050](https://doi.org/10.1051/0004-6361/202039050)
- Arnold, L. F. A. 2005, *ApJ*, 627, 534, doi: [10.1086/430437](https://doi.org/10.1086/430437)
- Ballard, S., Fabrycky, D., Fressin, F., et al. 2011, *ApJ*, 743, 200, doi: [10.1088/0004-637X/743/2/200](https://doi.org/10.1088/0004-637X/743/2/200)
- Barros, S. C. C., Akınanmi, B., Boué, G., et al. 2022, *A&A*, 657, A52, doi: [10.1051/0004-6361/202142196](https://doi.org/10.1051/0004-6361/202142196)
- Bastien, F. A., Stassun, K. G., Basri, G., & Pepper, J. 2013, *Nature*, 500, 427, doi: [10.1038/nature12419](https://doi.org/10.1038/nature12419)
- Baycroft, T. A., Triaud, A. H. M. J., Faria, J., Correia, A. C. M., & Standing, M. R. 2023, *MNRAS*, 521, 1871, doi: [10.1093/mnras/stad607](https://doi.org/10.1093/mnras/stad607)
- Benz, W., Broeg, C., Fortier, A., et al. 2021, *Experimental Astronomy*, 51, 109, doi: [10.1007/s10686-020-09679-4](https://doi.org/10.1007/s10686-020-09679-4)
- Bernabò, L. M., Csizmadia, S., Smith, A. M. S., et al. 2024, *A&A*, 684, A78, doi: [10.1051/0004-6361/202346852](https://doi.org/10.1051/0004-6361/202346852)
- Borucki, W. J., Koch, D., Basri, G., et al. 2010, *Science*, 327, 977, doi: [10.1126/science.1185402](https://doi.org/10.1126/science.1185402)
- Boyajian, T. S., LaCourse, D. M., Rappaport, S. A., et al. 2016, *MNRAS*, 457, 3988, doi: [10.1093/mnras/stw218](https://doi.org/10.1093/mnras/stw218)
- Brogi, M., Keller, C. U., de Juan Ovelar, M., et al. 2012a, *A&A*, 545, L5, doi: [10.1051/0004-6361/201219762](https://doi.org/10.1051/0004-6361/201219762)
- . 2012b, *A&A*, 545, L5, doi: [10.1051/0004-6361/201219762](https://doi.org/10.1051/0004-6361/201219762)
- Cabrera, J., Csizmadia, S., Lehmann, H., et al. 2014, *ApJ*, 781, 18, doi: [10.1088/0004-637X/781/1/18](https://doi.org/10.1088/0004-637X/781/1/18)
- Campante, T. L., Schofield, M., Kuzlewicz, J. S., et al. 2016, *ApJ*, 830, 138, doi: [10.3847/0004-637X/830/2/138](https://doi.org/10.3847/0004-637X/830/2/138)
- Caplan, M. E. 2019, *Acta Astronautica*, 165, 96, doi: [10.1016/j.actaastro.2019.08.027](https://doi.org/10.1016/j.actaastro.2019.08.027)
- Carado, B., & Knuth, K. 2020, *Astronomy and Computing*, 32, 100406, doi: [https://doi.org/10.1016/j.ascom.2020.100406](https://doi.org/https://doi.org/10.1016/j.ascom.2020.100406)
- Chakraborty, J., Wheeler, A., & Kipping, D. 2020, *MNRAS*, 499, 4011, doi: [10.1093/mnras/staa2928](https://doi.org/10.1093/mnras/staa2928)
- Claret, A. 2000, *A&A*, 363, 1081
- Correia, A. C. M. 2014, *A&A*, 570, L5, doi: [10.1051/0004-6361/201424733](https://doi.org/10.1051/0004-6361/201424733)

- Dyson, F. J. 1960, *Science*, 131,
doi: [10.1126/science.131.3414.1667](https://doi.org/10.1126/science.131.3414.1667)
- Espinoza, N., & Jordán, A. 2016, *MNRAS*, 457, 3573,
doi: [10.1093/mnras/stw224](https://doi.org/10.1093/mnras/stw224)
- Ferlet, R., Hobbs, L. M., & Vidal-Madjar, A. 1987, *A&A*, 185, 267
- Giles, H. A. C., Collier Cameron, A., & Haywood, R. D. 2017, *MNRAS*, 472, 1618, doi: [10.1093/mnras/stx1931](https://doi.org/10.1093/mnras/stx1931)
- Gillon, M., Triaud, A. H. M. J., Demory, B.-O., et al. 2017, *Nature*, 542, 456, doi: [10.1038/nature21360](https://doi.org/10.1038/nature21360)
- Hambleton, K., Kurtz, D. W., Prša, A., et al. 2016, *MNRAS*, 463, 1199, doi: [10.1093/mnras/stw1970](https://doi.org/10.1093/mnras/stw1970)
- Hambleton, K., Fuller, J., Thompson, S., et al. 2018, *MNRAS*, 473, 5165, doi: [10.1093/mnras/stx2673](https://doi.org/10.1093/mnras/stx2673)
- Haqq-Misra, J., Ashtari, R., Benford, J., et al. 2022, arXiv e-prints, arXiv:2209.11685,
doi: [10.48550/arXiv.2209.11685](https://doi.org/10.48550/arXiv.2209.11685)
- Harre, J.-V., & Smith, A. M. S. 2023, *Universe*, 9, 506,
doi: [10.3390/universe9120506](https://doi.org/10.3390/universe9120506)
- Hellard, H., Csizmadia, S., Padovan, S., et al. 2019, *ApJ*, 878, 119, doi: [10.3847/1538-4357/ab2048](https://doi.org/10.3847/1538-4357/ab2048)
- Kardashev, N. S. 1964, *Soviet Ast.*, 8, 217
- Kiefer, F., Van Grootel, V., Lecavelier des Etangs, A., et al. 2023, *A&A*, 671, A25, doi: [10.1051/0004-6361/202245104](https://doi.org/10.1051/0004-6361/202245104)
- Kipping, D., Bryson, S., Burke, C., et al. 2022, *Nature Astronomy*, 6, 367, doi: [10.1038/s41550-021-01539-1](https://doi.org/10.1038/s41550-021-01539-1)
- Koch, D. G., Borucki, W. J., Basri, G., et al. 2010, *ApJL*, 713, L79, doi: [10.1088/2041-8205/713/2/L79](https://doi.org/10.1088/2041-8205/713/2/L79)
- Kołaczek-Szymański, P. A., Pigulski, A., Michalska, G., Moździerski, D., & Różański, T. 2021, *A&A*, 647, A12,
doi: [10.1051/0004-6361/202039553](https://doi.org/10.1051/0004-6361/202039553)
- Kramm, U., Nettelmann, N., Fortney, J., Neuhäuser, R., & Redmer, R. 2012, *Astronomy & Astrophysics*, 538, A146
- Lebofsky, M., Croft, S., Siemion, A. P. V., et al. 2019, *Publications of the Astronomical Society of the Pacific*, 131, 124505, doi: [10.1088/1538-3873/ab3e82](https://doi.org/10.1088/1538-3873/ab3e82)
- Lecavelier Des Etangs, A., Vidal-Madjar, A., & Ferlet, R. 1996, *A&A*, 307, 542,
doi: [10.48550/arXiv.astro-ph/9508035](https://doi.org/10.48550/arXiv.astro-ph/9508035)
- Lipman, D., Isaacson, H., Siemion, A. P. V., et al. 2019, *PASP*, 131, 034202, doi: [10.1088/1538-3873/aafe86](https://doi.org/10.1088/1538-3873/aafe86)
- Loeb, A. 2023, *Research Notes of the American Astronomical Society*, 7, 43,
doi: [10.3847/2515-5172/acc10d](https://doi.org/10.3847/2515-5172/acc10d)
- Luger, R., Sestovic, M., Kruse, E., et al. 2017, *Nature Astronomy*, 1, 0129, doi: [10.1038/s41550-017-0129](https://doi.org/10.1038/s41550-017-0129)
- Maciejewski, G., Dimitrov, D., Fernández, M., et al. 2016, *A&A*, 588, L6, doi: [10.1051/0004-6361/201628312](https://doi.org/10.1051/0004-6361/201628312)
- Mandel, K., & Agol, E. 2002, *The Astrophysical Journal*, 580, L171–L175, doi: [10.1086/345520](https://doi.org/10.1086/345520)
- Maxted, P. F. L. 2016, *A&A*, 591, A111,
doi: [10.1051/0004-6361/201628579](https://doi.org/10.1051/0004-6361/201628579)
- Mayor, M., & Queloz, D. 1995, *Nature*, 378, 355,
doi: [10.1038/378355a0](https://doi.org/10.1038/378355a0)
- McKee, B., & Montet, B. 2024, in *AAS/Division for Extreme Solar Systems Abstracts*, Vol. 56, AAS/Division for Extreme Solar Systems Abstracts, 605.03
- Nachmani, G., Mazeh, T., & Sochen, N. 2022, *MNRAS*, 511, 5301, doi: [10.1093/mnras/stac135](https://doi.org/10.1093/mnras/stac135)
- NASA exoplanet science institute. 2010, *Exoplanet Archive*, doi: [10.26133/NEA5](https://doi.org/10.26133/NEA5)
- Ochsenbein F. et. al. 2000, *The VizieR database of astronomical catalogues*, doi: [10.26093/cds/vizieR](https://doi.org/10.26093/cds/vizieR)
- Rappaport, S., Levine, A., Chiang, E., et al. 2012, *ApJ*, 752, 1, doi: [10.1088/0004-637X/752/1/1](https://doi.org/10.1088/0004-637X/752/1/1)
- Rappaport, S., Vanderburg, A., Jacobs, T., et al. 2018, *MNRAS*, 474, 1453, doi: [10.1093/mnras/stx2735](https://doi.org/10.1093/mnras/stx2735)
- Ricker, G. R., Winn, J. N., Vanderspek, R., et al. 2015, *Journal of Astronomical Telescopes, Instruments, and Systems*, 1, 014003, doi: [10.1117/1.JATIS.1.1.014003](https://doi.org/10.1117/1.JATIS.1.1.014003)
- Sandford, E., & Kipping, D. 2019, *AJ*, 157, 42,
doi: [10.3847/1538-3881/aaf565](https://doi.org/10.3847/1538-3881/aaf565)
- Semiz, İ., & Oğur, S. 2015, arXiv e-prints, arXiv:1503.04376, doi: [10.48550/arXiv.1503.04376](https://doi.org/10.48550/arXiv.1503.04376)
- Smith, J. 2022, *PhyS*, 97, 122001,
doi: [10.1088/1402-4896/ac9e78](https://doi.org/10.1088/1402-4896/ac9e78)
- Steffen, J. H., Fabrycky, D. C., Ford, E. B., et al. 2012, *MNRAS*, 421, 2342,
doi: [10.1111/j.1365-2966.2012.20467.x](https://doi.org/10.1111/j.1365-2966.2012.20467.x)
- Svoronos, A. A. 2020, *Acta Astronautica*, 176, 306,
doi: [10.1016/j.actaastro.2020.07.005](https://doi.org/10.1016/j.actaastro.2020.07.005)
- Tarter, J. 2001, *ARA&A*, 39, 511,
doi: [10.1146/annurev.astro.39.1.511](https://doi.org/10.1146/annurev.astro.39.1.511)
- Tarter, J. C. 2007, *Highlights of Astronomy*, 14, 14,
doi: [10.1017/S1743921307009829](https://doi.org/10.1017/S1743921307009829)
- Tregloan-Reed, J., Southworth, J., & Tappert, C. 2013, *MNRAS*, 428, 3671, doi: [10.1093/mnras/sts306](https://doi.org/10.1093/mnras/sts306)
- Vivekananda Rao, P., Sarma, M. B. K., & Prakash Rao, B. V. N. S. 1991, *Journal of Astrophysics and Astronomy*, 12, 225, doi: [10.1007/BF02702880](https://doi.org/10.1007/BF02702880)
- Wright, J. T. 2020, *Serbian Astronomical Journal*, 200, 1,
doi: [10.2298/SAJ2000001W](https://doi.org/10.2298/SAJ2000001W)
- Wright, J. T., Cartier, K. M. S., Zhao, M., Jontof-Hutter, D., & Ford, E. B. 2016, *ApJ*, 816, 17,
doi: [10.3847/0004-637X/816/1/17](https://doi.org/10.3847/0004-637X/816/1/17)
- Wright, J. T., Haqq-Misra, J., Frank, A., et al. 2022, *ApJL*, 927, L30, doi: [10.3847/2041-8213/ac5824](https://doi.org/10.3847/2041-8213/ac5824)
- Yu, J., Huber, D., Bedding, T. R., et al. 2018, *ApJS*, 236, 42, doi: [10.3847/1538-4365/aaaf74](https://doi.org/10.3847/1538-4365/aaaf74)

Zuckerman, A., Davenport, J. R. A., Croft, S., Siemion, A.,
& de Pater, I. 2024, *AJ*, 167, 20,
doi: [10.3847/1538-3881/acfa6c](https://doi.org/10.3847/1538-3881/acfa6c)

Zuluaga, J. I., Sucerquia, M., & Alvarado-Montes, J. A.
2022, *Astronomy and Computing*, 40, 100623,
doi: [10.1016/j.ascom.2022.100623](https://doi.org/10.1016/j.ascom.2022.100623)